Unravelling Species-Specific Loading Effects on Oxygen Reduction Activity of Heteronuclear Single Atom Catalysts

Tong Yang[a], Keda Ding[a], Jun Zhou[b], Xiaoyang Ma[c], Kay Chen Tan[d], Ge Wang[e], Haitao Huang[a], and Ming Yang [a, *]

[a] Department of Applied Physics, The Hong Kong Polytechnic University, Hung Hom, Hong Kong SAR, China

[b] Institute of Materials Research and Engineering (IMRE), Agency for Science, Technology and Research (A*STAR), 2 Fusionopolis Way, Innovis #08-03, Singapore 138634, Republic of Singapore

[c] School of Information Science and Engineering, Shandong University, 72 Binhai Road, Qingdao 266237, China

[d] Department of Computing, The Hong Kong Polytechnic University, Hung Hom, Hong Kong SAR, China

[e] Beijing Advanced Innovation Center for Materials Genome Engineering, Beijing Key Laboratory of Function Materials for Molecule & Structure Construction, School of Materials Science and Engineering, University of Science and Technology Beijing, Beijing 100083, China

[*] To whom the correspondence should be addressed: mingyang@polyu.edu.hk (M. Y.)

Abstract

Toward high-density single atom catalysts (SACs), the interaction between neighboring SACs and the induced non-linear loading effect become crucial for their intrinsic catalytic performance. Despite recent investigations on homonuclear SACs, understanding such effect in heteronuclear SACs remains limited. Using Fe and Co SACs co-supported on the nitrogen-doped graphene as a model system, the loading effect on the site-specific activity of heteronuclear SACs toward oxygen reduction reaction (ORR) is here reported by density functional theory calculations. The Fe site exhibits an oscillatory decrease in activity with the loading. In contrast, the Co site has a volcano-like activity with the optimum performance achieved at ≈16.8 wt.% (average inter-site distance: ≈7 Å). At the ultra-high loading of 38.4 wt.% (inter-site distance: ≈4 Å), the Co site is the only ORR active site, whereas Fe sites turn into spectators. This distinct loading-dependent activity between the Fe and Co sites can be ascribed to their difference in the binding capability with the substrate and the dxz and d yz orbitals' occupation. These findings highlight the importance of the loading effect in heteronuclear SACs, which could be useful for the development of high-performance heteronuclear and high-entropy SACs toward various catalytic reactions in the high-loading regime.

Introduction

Single atom catalysts (SACs) have received tremendous attention due to the maximum atom utilization, high catalytic activity and unique selectivity.[1-3] Over the past decade, SACs have been reported to exhibit high catalytic performance towards various electrochemical reactions, such as hydrogen evolution reaction (HER),[4-9] oxygen evolution/reduction reaction (OER/ORR),[10-14] nitrogen reduction reaction (NRR)[15-18] and carbon dioxide reduction reaction (CO_2RR).[19, 20] Amounts of efforts have also been put in engineering the local coordination environment of SACs, aiming to further fine-tune or modify their intrinsic catalytic performance.[20-28] For instance, four-fold carbon-embedded nitrogen coordinated iron and cobalt single atoms (FeN_4-C and CoN_4-C) are well-known for their high activity and selectivity towards the $4e^-$ ORR pathway to water (H_2O) and have been proposed as promising alternatives to noble metal based electrocatalyst platinum (Pt).[10, 11] The catalytic activity of FeN_4-C can be further enhanced upon selective cleavage of adjacent C-N bonds or phosphorous doping.[21, 22] As for CoN_4-C, either deliberate substitutions of the nitrogen atoms with oxygen dopants or the presence of oxygen adsorbates near the CoN_4 moiety could shift its catalytic selectivity towards the $2e^-$ ORR pathway to hydrogen peroxides (H_2O_2).[24, 25]

Apart from the intrinsic activity of SACs, increasing their loading is also of great importance to meet the overall performance criteria. Although it is extremely challenging due to the high surface free energy and low coordination number of SACs, substantial progress has been made. Wan *et. al.* recently managed to synthesize the concave-shaped FeN_4-C with the Fe loading of up to 2.78 wt% and showed that its ORR catalytic performance could achieve the US Department of Energy 2018 target set for platinum-group metal-free catalysts in proton exchange membrane fuel cells.[29] Such an achievement was mainly contributed by the enhanced mass transport and the high density of exposed Fe active sites. Subsequent experimental studies reported that the Fe loading of FeN_4-C could further increase up to 7~8 wt%.[30, 31] Furthermore, Hai *et. al.* recently demonstrated a general two-step annealing method for preparing ultra-high-density SACs, through which the Fe loading of FeN_4-C can be even pushed to as high as ~14.6 wt%.[32] It is noteworthy that the overall catalytic performance of SACs may not always scale linearly with the single atom loading. In particular, in the high loading regime, individual single atom sites come closer and hence are likely to interact with one another, leading to a pronounced dependence of the site-specific activity on the loading. Such loading effect has been experimentally observed on FeN_4-C.[33] Wherein, the intrinsic site-specific ORR activity was found to start increasing from 1.82 wt% until the Fe loading reaches 5.41 wt%, above

which it is slightly diminished. Analogously, the polymeric carbon nitride with highly loaded Cu single atoms (~22 wt% Cu) shows a seven times higher site-specific activity than the low loaded counterpart (1.0 wt% Cu) for the azide-alkyne cycloaddition reaction of 4-ethynylanisole with benzyl azide.[32] In contrast, the Ni SACs supported on nitrogen-doped carbon lose ~30% of the per-site activity as the Ni loading increases from 1.6 wt% to 16.3 wt%.[32] These experimental findings manifest the crucial yet subtle nature of the loading effect on the site-specific activity in the high loading regime. It is also noted that these studies mainly focus on the homonuclear SACs.

On the other hand, engineering the atomic species of neighbouring single atoms and forming heteronuclear SACs brings a considerable impact on the intrinsic activity of the single atom of each species. In spite of the greater challenge than synthesis of highly loaded homonuclear SACs, co-doping single atoms of two or more species into the same substrate has been recently realized in experiments, such as Ni and Pd single atoms co-supported by nitrogen-doped carbon with the total metal loading of 12.8 wt% and the 12-metal mixed SACs (Sc, Mn, Fe, Co, Ni, Cu, Zn, Y, Zr, Pd, Hf and W) with the total metal loading of 7.52 wt%.[32, 34] Intriguingly, the multi-element synergistic interaction was found to be able to significantly enhance the catalytic activity compared with the monometallic SACs.[34] Bearing in mind the pronounced loading effect for homonuclear/monometallic SACs, one important question is naturally raised for heteronuclear/multimetallic SACs: what effect does the loading have on the multi-element interaction or the site-specific activity of the constituent single atom of each species in the high loading regime? Noting the superior performance of FeN_4-C and CoN_4-C towards the $4e^-$ ORR pathway,[10, 11] in this study, they were chosen as a model system of heteronuclear SACs to systematically investigate loading effect on the intrinsic site-specific ORR activity of each constituent single atom in the high loading regime.

Results and Discussion

Structural Models and Stability

To scrutinize the loading effect on the intrinsic site-specific activity, a pair of heteronuclear TMN_4 moieties (TM=Fe, Co) were accommodated by the graphene substrate. The total metal loading considered ranges from ~3 wt% to ~17 wt%, which was simulated by adjusting the supercell size ($n\times n$) of the graphene substrate. A recent study suggests that at the high metal loading of 14.3 wt%, the further apart are the Fe and Co single atoms, the more energetically stable the heteronuclear SACs are.[35] Therefore, two kinds of configurations with an nearly

equally furthest inter-site distance (d_{site}) were considered at a given TM loading (**Figure S1** in Supporting Information). As shown in **Figures 1a-b** for the TM loading of 16.8 wt%, which corresponds to the 5×5 graphene substrate supercell, one moiety ($TM_{cen}N_4$) is located near the centre of the model and the other ($TM_{cor}N_4$) near the corner. In configuration I (II), the line connecting TM_{cen} and TM_{cor} is parallel to (slightly deviates from) the diagonal, which is hereafter denoted as TM_{cen}-TM_{cor}@n×n-I (TM_{cen}-TM_{cor}@n×n-II). **Figure 1c** displays the average distance between the neighbouring Fe_{cen} and Co_{cor} sites ($\langle d_{\mathrm{site}} \rangle$), which ranges from ~7 Å to ~16 Å. Meanwhile, a 9×9 graphene supercell with one TMN_4 moiety embedded, which has $\langle d_{\mathrm{site}} \rangle$ of 22.21 Å and is denoted as TMN_4@9×9-S, was here used to simulate the isolated TMN_4-C. It should be noted that the simulation models adopted here may give an average upper bound of the metal loading. In the experimentally grown samples, there usually exist pores and nitrogen dopants which have yet anchored any single TM atoms. As manifested by Ref. 33 [33], the experimentally synthesized FeN_4-C samples have an average inter-site distance of 5 Å, 7 Å and 12 Å based on the statistical analysis of the STEM images, whereas the corresponding metal loadings estimated by ICP-MS are only 8.02 wt%, 5.41 wt% and 1.82 wt%, respectively.

The stability of Fe_{cen}-Co_{cor}@n×n was first examined. As shown in **Figure 1c**, our calculations indicated that configuration II is more energetically stable than configuration I across the concerned loading range. The energy difference between configuration I and II, $E(n \times n - \mathrm{I}) - E(n \times n - \mathrm{II})$, reaches the maximum at $n = 7$ (9.1 wt% TM), above which it quickly drops. Such a quick drop somewhat indicates that the loading effect (inter-site interaction between Fe_{cen} and Co_{cor}) might become very weak or negligible when the metal loading (the average inter-site distance) is below 3.8 wt% (above ~16 Å).

The thermodynamic and electrochemical stabilities of Fe_{cen}-Co_{cor}@n×n can be further evaluated by the formation energy (E_f) and the dissolution potential (U_d) as follows:

$$E_{\mathrm{f}}(\mathrm{TM}) = E(tot) - E(\mathrm{V_{TM}}) - E(\mathrm{TM_{bulk}}) \qquad (1)$$

$$U_{\mathrm{d}}(\mathrm{TM}) = U_{\mathrm{d}}^{\mathrm{o}}(\mathrm{TM_{bulk}}) - \frac{E_{\mathrm{f}}(\mathrm{TM})}{Ne} \qquad (2)$$

where $E(tot)$ and $E(\mathrm{V_{TM}})$ are the total energy of Fe_{cen}-Co_{cor}@n×n without and with a TM vacancy (V_{TM}; TM=Fe_{cen} or Co_{cor}), respectively. $E(\mathrm{TM_{bulk}})$ is the per-atom energy of the bulk-phase TM. $U_{\mathrm{d}}^{\mathrm{o}}(\mathrm{TM_{bulk}})$ is the standard dissolution potential of the bulk-phase TM and N the number of electrons involved in the dissolution. It has been reported that $E_{\mathrm{f}}(\mathrm{TM}) < 0$ eV and $U_{\mathrm{d}}(\mathrm{TM}) > 0$ V hold for most experimentally synthesized SACs.[36] Therefore, we applied this

set of stability criteria, as summarized in **Figure 1d**. It can be seen that all Fe_{cen}-Co_{cor}@n×n-II considered in this work meet the criteria, implying their stability against aggregation and dissolution. With the increasing TM loading, the formation energy (the dissolution potential) of both Fe_{cen} and Co_{cor} increases (decreases), suggesting a lower stability when they are approaching one another. This explains the experimental observations that synthesizing high-density SACs remains challenging.[3] In addition, the lower formation energy of Co_{cor} than that of Fe_{cen} may suggest a stronger binding interaction with the neighbouring nitrogen dopants, which is consistent with the shorter Co_{cor}-N bonds (see **Figure S2**). Hereafter, we will focus on the more stable Fe_{cen}-Co_{cor}@n×n-II ($n = 9, 7, 5$) and TM@9×9-S.

Site-Specific ORR Catalytic Activities of Fe_{cen}-Co_{cor}@n×n-II

Prior to explorations of the loading-dependent site-specific ORR activity, we studied the catalytic activity of isolated FeN_4-C and CoN_4-C using Fe@9×9-S (2.8 wt% Fe) and Co@9×9-S (3.0 wt% Co), respectively, where the inter-site distance is above 20 Å (**Figure 1c**). **Figures 2a** and **3a** display the calculated Gibbs free energy diagram along the 4e^- ORR pathway on the isolated Fe and Co sites, respectively. The lower Gibbs free energy suggests that the Fe site tends to adsorb all intermediate adsorbates more strongly than the isolated Co site, especially the *O adsorbate. This may be ascribed to the relatively stronger binding of the later with the graphene substrate (see **Figure 1d**). For the isolated Fe site, the hydrogenation of *O to *OH turns out to be the potential-determining step (PDS), whereas it is the first hydrogenation to *OOH for the Co site. As an effective thermodynamic descriptor, the limiting potential (U_L) is calculated to be 0.980 V for the Fe site and 0.925 V for the Co site. This implies the high ORR catalytic activity of both single SACs at the low loading regime, between which the Fe SAC is better. It is noteworthy that the superior ORR catalytic activities of Fe and Co SACs and their relative activity trend of Fe SACs > Co SACs have been widely observed in experiments.[10, 11, 29, 37-39] These agreements suggest the reliability of our calculations. We also note that Fe@9×9-S corresponds to a Fe loading of 2.8 wt%, which is very similar to that of the previously synthesized concave-shaped FeN_4-C (2.78 wt% Fe) with the observed superior ORR performance.[29]

The loading effect on the Fe site of Fe_{cen}-Co_{cor}@n×n was then investigated. For clarity, TM_{cen} and TM_{cor} of TM_{cen}-TM_{cor}@n×n are hereafter denoted as TM_{cen}@n×n and TM_{cor}@n×n, respectively. **Figures 2b-d** illustrate the calculated Gibbs free energy along the 4e^- ORR

pathway for Fe_{cen}@n×n-II at the metal loading of 5.7 wt%, 9.1 wt% and 16.8 wt%, respectively. As the metal loading increases from 2.8 wt% to 5.7 wt%, our calculations suggest a slight modulation on the energetics of ORR intermediate adsorbates. Although PDS is shifted from the hydrogenation of *O to *OH (**Figure 2a**) to that of *OH to H_2O (**Figure 2b**), the calculated limiting potential of Fe_{cen}@9×9-II ($U_L = 0.990$ V) is very similar to that of Fe@9×9-S ($U_L = 0.980$ V). This indicates that the change in the catalytic performance towards ORR is likely negligible. This may be because at such a loading, the neighbouring Co sites are still too far away (~13 Å) to interact with the Fe site. As the metal loading further increases to 9.1 wt% TM (Fe_{cen}-Co_{cor}@7×7-II), however, the binding strength of *OH on the Fe site is excessively increased to 0.445 eV (**Figure 2c**). Therefore, PDS of the ORR process on the Fe site remains the hydrogenation of *OH but the dramatically strengthened *OH adsorption leads to a significant decrease in the limiting potential from 0.990 V to 0.445 V and thus a substantial decrease in the ORR catalytic activity. **Figure 2d** shows that *OH adsorption becomes even stronger as the metal loading continues increasing, resulting in further catalytic performance deterioration of the Fe site.

As for Co_{cor}@n×n-II, **Figure 3** shows that PDS for the 4e^- ORR pathway remains unchanged across the concerned loading range – the hydrogenation of O_2 to *OOH. Notably, the adsorption strength of *OOH on the Co site keeps being enhanced as the metal loading increases from 3.0 wt% to 16.8 wt%. As a result, the calculated limiting potential monotonically increases, implying the enhanced intrinsic ORR activity of the Co site. This is in stark contrast to Fe_{cen}@n×n-II, where the loading effect is found negative for its intrinsic ORR activity. At the loading of 16.8 wt%, in particular, the limiting potential of the Co site is calculated to be $U_L = 1.022$ V, which is even higher than that of the nearly isolated Fe@9×9-S ($U_L = 0.980$ V) and Fe_{cen}@9×9-II ($U_L = 0.990$ V).

Mechanism of the Site-Specific Activity of Fe_{cen}-Co_{cor}@n×n-II

Note that both Fe and Co are magnetic elements and previous investigations have suggested that either Fe or Co in different spin state is likely to exhibit different catalytic performances.[40-45] Therefore, we analysed the spin state of Fe_{cen} and Co_{cor} in Fe_{cen}-Co_{cor}@n×n-II, in particular when the potential-determining ORR intermediate adsorbate is present. Before the ORR process, our calculations show that Fe_{cen}@n×n-II and Co_{cor}@n×n-II have a nearly constant magnetic moment of around 2 μ_B and 1 μ_B, respectively, regardless of the metal loading considered here. They are respectively very similar to those of the Fe and Co atoms in Fe@9×9-

S and Co@9×9-S. As for Fe_{cen}@n×n-II, since *OH adsorption is the potential-determining intermediate adsorbate across n in the metal loading range from 5.7 wt% to 16.8 wt% (see **Figure 2**), the spin state of Fe_{cen} with *OH adsorbed was studied and summarized in **Figure 4a**. In the presence of the *OH adsorbate on Fe_{cen}, its magnetic moment exhibits a step-like transition with the increase in the metal loading. The low-spin state of Fe_{cen} remains until the metal loading reaches 9.1 wt% (Fe_{cen}-Co_{cor}@7×7-II), above which Fe_{cen} is in a high-spin state. It is noted that this step-like transition essentially occurs at the same metal loading as the excessive strengthening of *OH adsorption ($G(*\mathrm{OH})$) or significant deterioration of the ORR activity of Fe_{cen}. Analogous to Fe@9×9-S, the adsorption of *OOH – the potential-determining intermediate adsorbate of the Co site – significantly reduces the magnetic moment of Co@9×9-S compared with the pristine counterpart at the metal loading of 3.0 wt%, as shown in **Figure 4b**. Also, there is a significant increase in the magnetic moment of Co_{cen} but it starts earlier at 5.7 wt% TM. Afterwards, the magnetic moment of Co_{cor} continuously increases with the metal loading. We note that a similar trend is observed for the loading-dependent ORR activity of the Co site (**Figure 4b**).

Further analyses show that the above similar loading-dependent catalytic activity and magnetic moment may be linked to the local structural evolution. In the absence of *OH (*OOH), the Fe (Co) site always lies within the graphene substrate plane, which may be responsible for the aforementioned loading independent spin state. Upon *OH (*OOH) adsorption, however, the Fe (Co) atom is likely pulled out of the graphene substrate, breaking the independence. **Figure 4** summarizes the loading dependence of the bond length between the Fe (Co) atom and the (nearest) oxygen atom of *OH (*OOH), $d_{\mathrm{Fe-O}}$ ($d_{\mathrm{Co-O}}$), as well as the protrusion height of the Fe (Co) atom, h_{Fe} (h_{Co}). For *OH adsorption on Fe_{cen}, the Fe-O bond length only varies slightly, whereas Fe_{cen} starts to significantly protrude from the graphene substrate plane at the metal loading of 9.1 wt% (Fe_{cen}-Co_{cor}@7×7-II), above which the high protrusion remains. On the one hand, such a significant protrusion from 9.1 wt% and onwards may explain the excessive enhancement of *OH adsorption on Fe_{cen} and hence the deterioration of its intrinsic ORR activity (see **Figures 2** and **4a**). On the other hand, it indicates the local environment transition of Fe_{cen} from the in-planar coordination to the tetrahedral one at the metal loading of 9.1 wt%, thereby causing the transition towards the high-spin state.[44] Contrary to Fe_{cen}, **Figure 4b** shows that the adsorption of *OOH leads to a nearly constant small protrusion across the considered metal loading range, whereas the Co-O bond length keeps increasing with the metal

loading, which seems to positively correlate with the increased magnetic moment and the limiting potential of the Co site.

The electronic structure of the Fe and Co site was also investigated in order to gain a deeper insight into the loading-dependent intrinsic ORR activity as well as the accompanied spin state evolution. Fe@9×9-S, Co@9×9-S and Fe_{cen}-Co_{cor}@5×5-II were chosen as representative systems. As shown in **Figure S3**, the Fe sites of Fe@9×9-S and Fe_{cen}-Co_{cor}@5×5-II show similar electronic structures without ORR intermediate adsorbates, due to the similar in-planar coordination environment. The constant magnetic moment of 2 μ_B is contributed by the nearly empty Fe-d_{z^2} orbital and the partially occupied Fe-d_{xz} and d_{yz} orbitals in the spin-down channel (**Figure S3**). Upon adsorption of *OH on Fe@9×9-S, the spin-up Fe-d_{z^2} orbital couples to the molecular state of *OH and forms partially unoccupied anti-bonding state in the spin-up channel, thereby giving rise to the reduced magnetic moment of the Fe site in 9×9-S (**Figure 5b**). As the metal loading increases to 16.8 wt% (Fe_{cen}-Co_{cor}@5×5-II), the significant adsorption-induced protrusion causes a large spin splitting for all Fe-*d* orbitals, leading to more (less) unoccupied spin-down (spin-up) states and thus the high-spin state (**Figure 5a**). It is worth noting that the strong splitting also significantly pushes the occupied hybridized states downwards in energy, leading to the excessively strong adsorption of *OH on Fe_{cen} as the metal loading increases.

As for the pristine Co site of Co@9×9-S and Fe_{cen}-Co_{cor}@5×5-II, **Figure S4** shows that their electronic structures are also very similar to one another, where the constant magnetic moment of 1 μ_B stems from the empty Co-d_{z^2} orbital in the spin-down channel. When the potential-determining *OOH adsorbs, the hybridization with the molecular states of *OOH reduces the spin polarization of the Co-d_{z^2} orbital with the spin-up (spin-down) channel partially unoccupied (occupied) (**Figure 6b**). The visualized partial charge in **Figure S5** reveals the anti-bonding nature of the first peak below the Fermi level (in the green-shaded area of **Figure 6b**), which suggests the fractional occupation of the anti-bonding state at the loading of 3.0 wt% (Co@9×9-S). From **Figures 6a and S5**, one can see that more anti-bonding states are occupied at the loading of 16.8 wt% (Fe_{cen}-Co_{cor}@5×5-II). These occupied anti-bonding states are spin polarized and are likely responsible for the increase in the magnetic moment of the Co site (see **Figure 4b**). On the other hand, while the occupied anti-bonding states increase with the metal loading, our calculations show strengthened adsorption of the potential-determining *OOH on the Co site (**Figures 3** and **4b**). In this regard, the significant elongation of the Co-O bond may play a key role (**Figure 4b**).

Hydroxyl Passivation and Ultra-High Loading of Fe_{cen}-Co_{cor}@*n*×*n*

Investigations have shown that FeN_4-C with an axial nitrogen ligand (N-FeN_4-C) is also active towards ORR, where the nitrogen ligand draws the Fe atom out of plane, forming a tetrahedral coordination.[43, 44] Noting the strong adsorption of *OH on the Fe site and the similar tetrahedral coordination environment at the metal loading of 9.1 wt% and 16.8 wt% (**Figure 4a**), the first *OH adsorbate on the Fe site may act as an axial ligand as well. As shown in **Figure 7**, the hydroxyl-passivated Fe site indeed binds all ORR intermediate adsorbates less strongly, especially the *O and *OH adsorbates. As such, the potential-determining step is shifted to the first hydrogenation step and the calculated limiting potential is increased from 0.445 V to 0.786 V at 9.1 wt% and from 0.405 V to 0.910 V at 16.8 wt% (**Figures 7** and **4a**). This result may suggest that when the metal loading is at 9.1 wt% or above, the ORR active site would transform from the pristine Fe site to the hydroxyl-passivated one.

This propensity of the Fe site to the hydroxyl passivation is further confirmed at the ultra-high metal loading of 38.4 wt%, of which the corresponding simulation model (Fe_{cen}-Co_{cor}@3×3) is depicted in **Figure 8a**. The formation energy and the dissolution potential were calculated to be -1.663 eV and 0.381 V for the Fe site, and -1.779 eV and 0.610 V for the Co site. This is consistent with the trend of stability being decreased with the metal loading observed in **Figure 1d**. Nevertheless, they still meet the aforementioned criteria and are stable against aggregation and dissolution. For the Gibbs free energy calculations, Fe_{cen}-Co_{cor}@3×3 is in-plane doubled. From **Figure 8b**, it is clear that the adsorption of the potential-determining *OH on the Fe site becomes even more stronger than that at the metal loading of 16.8 wt% (**Figure 2d**). With the first *OH adsorbate being the axial ligand, the potential-determining step is again shifted to the first hydrogenation step and the calculated limiting potential is increased to 0.676 V (**Figure 8b**). As for the Co site, the weakened binding to the graphene substrate in turn leads to an excessive adsorption enhancement of all intermediate adsorbates compared with those at 16.8 wt% (**Figures 8c** and **3d**). As a result, the ORR potential-determining step of the Co site is shifted to the hydrogenation of *O to *OH and the intrinsic catalytic activity is lowered with the limiting potential of 0.632 V.

Based on the above analyses, the Fe and Co site of heteronuclear Fe_{cen}-Co_{cor}@*n*×*n* exhibit very different dependence on the metal loading. For the Co site, its intrinsic ORR activity can be expected to first increase and peak at the metal loading of around 16.8 wt%, above which it is significantly decreased (**Figures 4b** and **8c**). On the contrary, the intrinsic ORR activity of the

Fe site decreases in an oscillatory manner with the metal loading (**Figures 4a** and **8b**). It is worth noting that such an oscillatory decrease is different from the intrinsic site-specific ORR activity of the Fe site in the homonuclear Fe SACs. In the latter case, the site-specific intrinsic activity of the high-density Fe SACs was experimentally found to be volcano-like with the highest reached at the average inter-site distance of about 7 Å.[33] Such inter-site distance is very analogous to that of Fe_{cen}-Co_{cor}@9×9-II at the metal loading of 16.8 wt% in the present study (**Figure 1c**). Therefore, the loading effect on the site-specific intrinsic activity of heteronuclear SACs is essentially species-specific and dependent on the atomic species of the co-supported single atoms.

Among the sites considered above, the Co site of Fe_{cen}-Co_{cor}@5×5-II was found to be the most active site (**Figure 4**). We further substituted Fe_{cen} in this configuration with Mn, Co, Ni, Cu, Ir and Pt, and investigated the catalytic activity of Co_{cor}. In the single atom form, these elements have been reported experimentally synthesizable and stable during the ORR process.[23, 46-49] The calculated Gibbs free energy diagrams are displayed in **Figure S6** and **Figure 8d** summarizes the associated limiting potential. One can see that the Pt_{cen} substitution can further improves the catalytic activity of Co_{cor}, whereas it slightly decreases when Fe_{cen} is replaced with Mn_{cen}, Co_{cen} and Ir_{cen}.

Conclusion

In summary, we systematically investigated the loading effect on stability and the site-specific ORR activity of heteronuclear Fe and Co SACs co-supported on the nitrogen-doped graphene in the high loading regimes. It is found that once synthesized, Fe_{cen}-Co_{cor}@n×n is likely stable against aggregation and dissolution. Our calculations also indicate the distinct loading-dependent intrinsic ORR activity of the Fe and Co site. The intrinsic activity of the Co site exhibits a volcano-like dependence on the metal loading with the highest reached at around 16.8 wt% TM. On the contrary, the Fe site tends to undergo the hydroxyl passivation and experiences an oscillatory decrease in the intrinsic ORR activity as the metal loading increases. By taking into consideration both metal loading and the site-specific ORR activity, the heteronuclear Fe and Co SACs may achieve the highest overall ORR performance at the metal loading of around 16.8 wt%. These results demonstrate that the loading effect of heteronuclear SACs is essentially not only specific to the species of the active site, but also dependent on the species of the co-supported single atom. Our work provides a deep understanding of the loading

effects of heteronuclear SACs on the electrocatalytic performance and may stimulate further investigations on the loading effect of other heteronuclear SACs of two or more atomic species, or even concentration-complex heteronuclear SACs.

Conflicts of Interest

There are no conflicts to declare.

Acknowledgements

This work was supported by the Hong Kong Polytechnic University (project ID: 1-BE47 and ZE2F). W. G. thanked National Natural Science Foundation of China (NSFC) for the financial support (No. 51972024). We acknowledged the Centre for Advanced 2D Materials and Graphene Research and the High-Performance Computing Centre at the National University of Singapore, and the National Supercomputing Centre of Singapore for providing the computing resources.

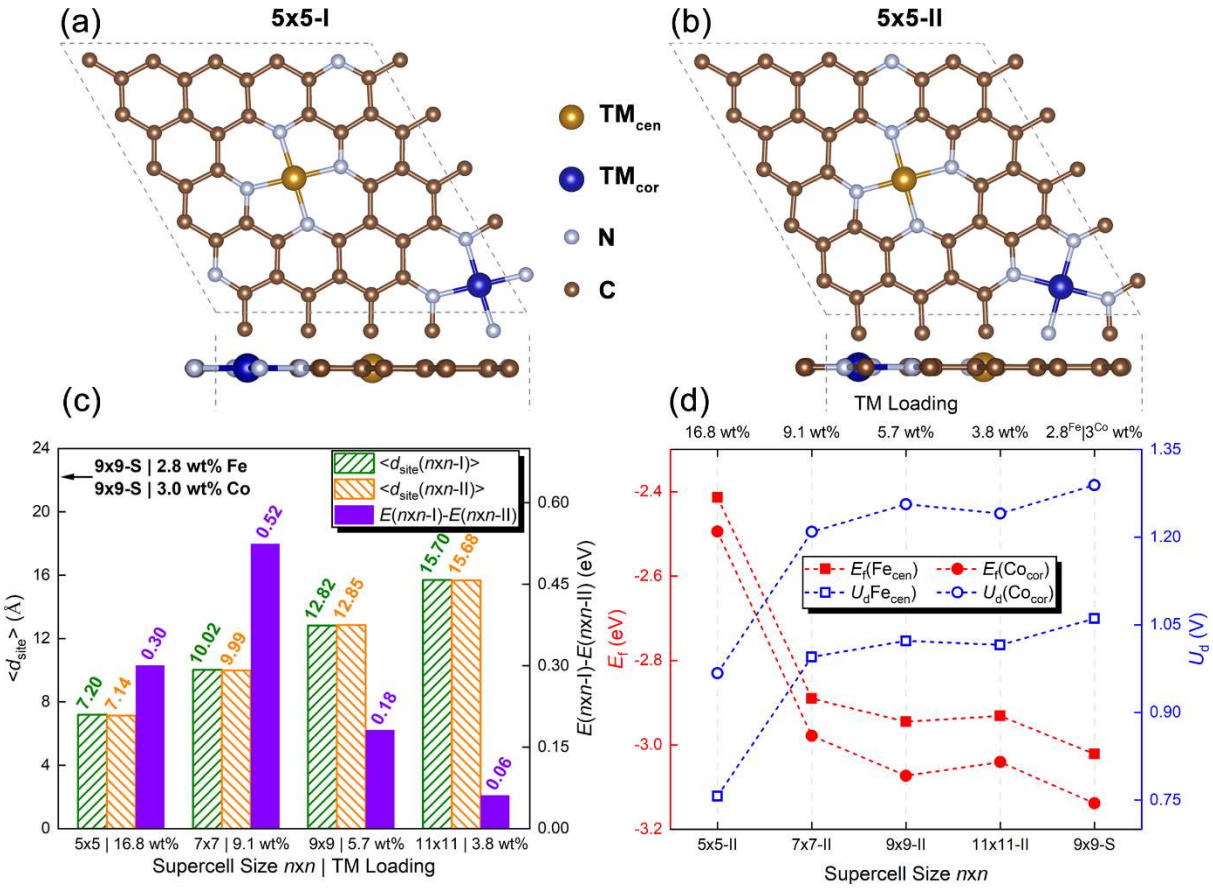


Figure 1. (a-b) The top (top row) and side view (bottom row) of (a) TM_{cen}-TM_{cor}@n×n-I and (b) TM_{cen}-TM_{cor}@n×n-II at $n = 5$ with the TM loading of 16.8 wt%. (c) The average distance between Fe_{cen} and Co_{cor} ($\langle d_{site} \rangle$) and the relative energetic stability between Fe_{cen}-Co_{cor}@n×n-I and Fe_{cen}-Co_{cor}@n×n-II, E(n×n-I)- E(n×n-II), as functions of the supercell size (TM loading). (d) The formation energy and the dissolution potential of Fe_{cen} and Co_{cor} as functions of the supercell size (TM loading).

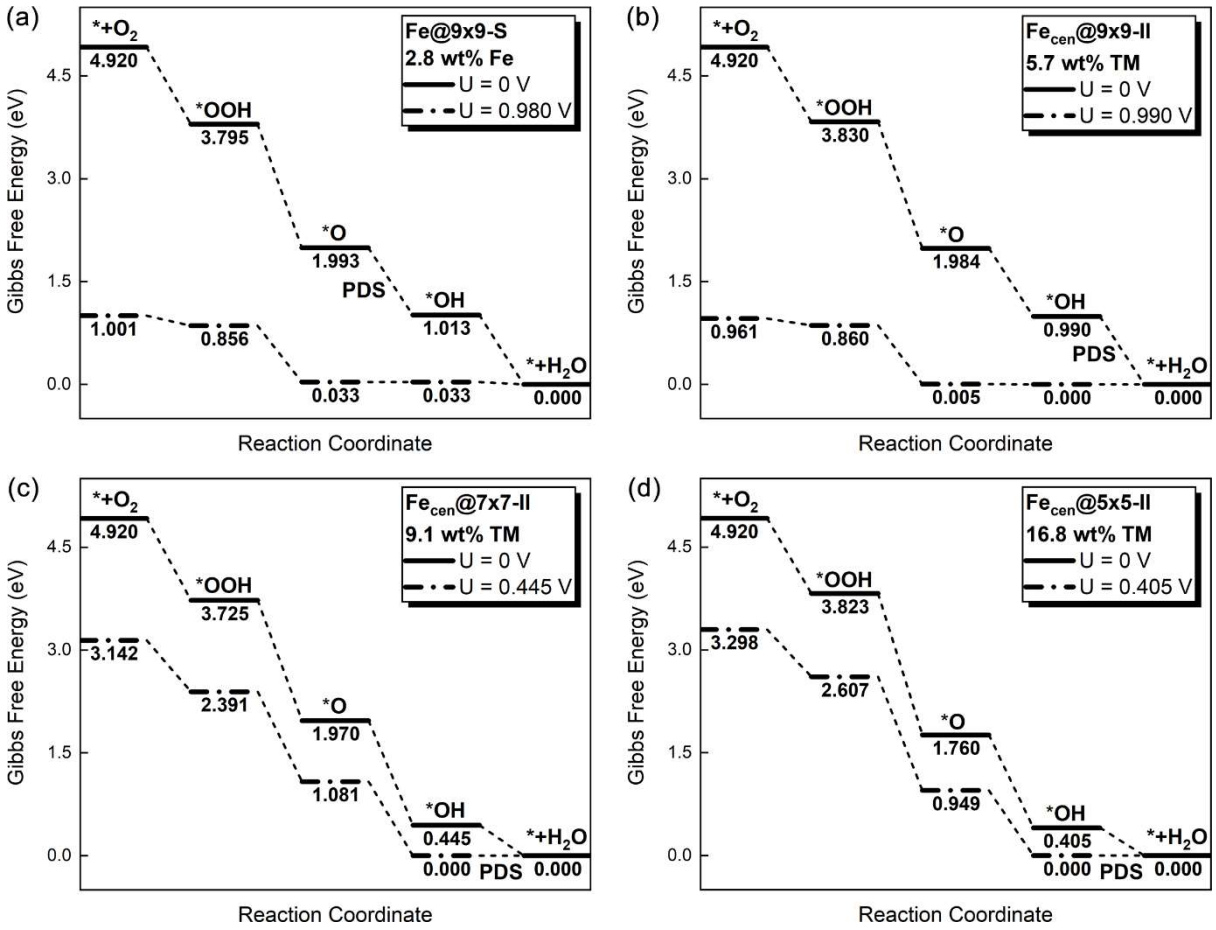


Figure 2. (a-b) The Gibbs free energy diagram for oxygen reduction reaction on the Fe site of (a) Fe@9×9-S, (b) Fe_{cen}-Co_{cor}@9×9-II, (c) Fe_{cen}-Co_{cor}@7×7-II and (d) Fe_{cen}-Co_{cor}@5×5-II. The corresponding TM loadings are marked.

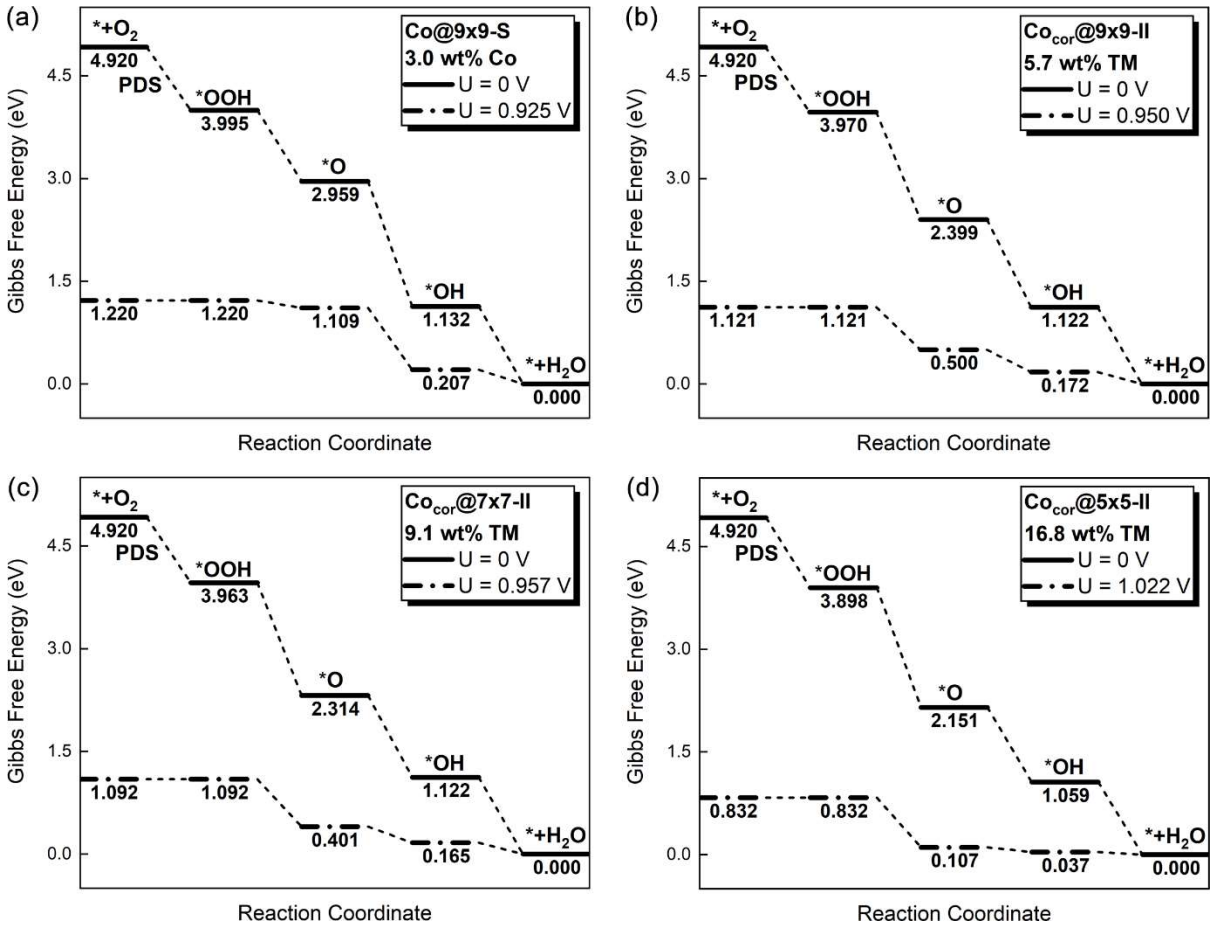


Figure 3. (a-b) The Gibbs free energy diagram for oxygen reduction reaction on the Co site of (a) Co@9×9-S, (b) Fe_{cen}-Co_{cor}@9×9-II, (c) Fe_{cen}-Co_{cor}@7×7-II and (d) Fe_{cen}-Co_{cor}@5×5-II. The corresponding TM loadings are marked.

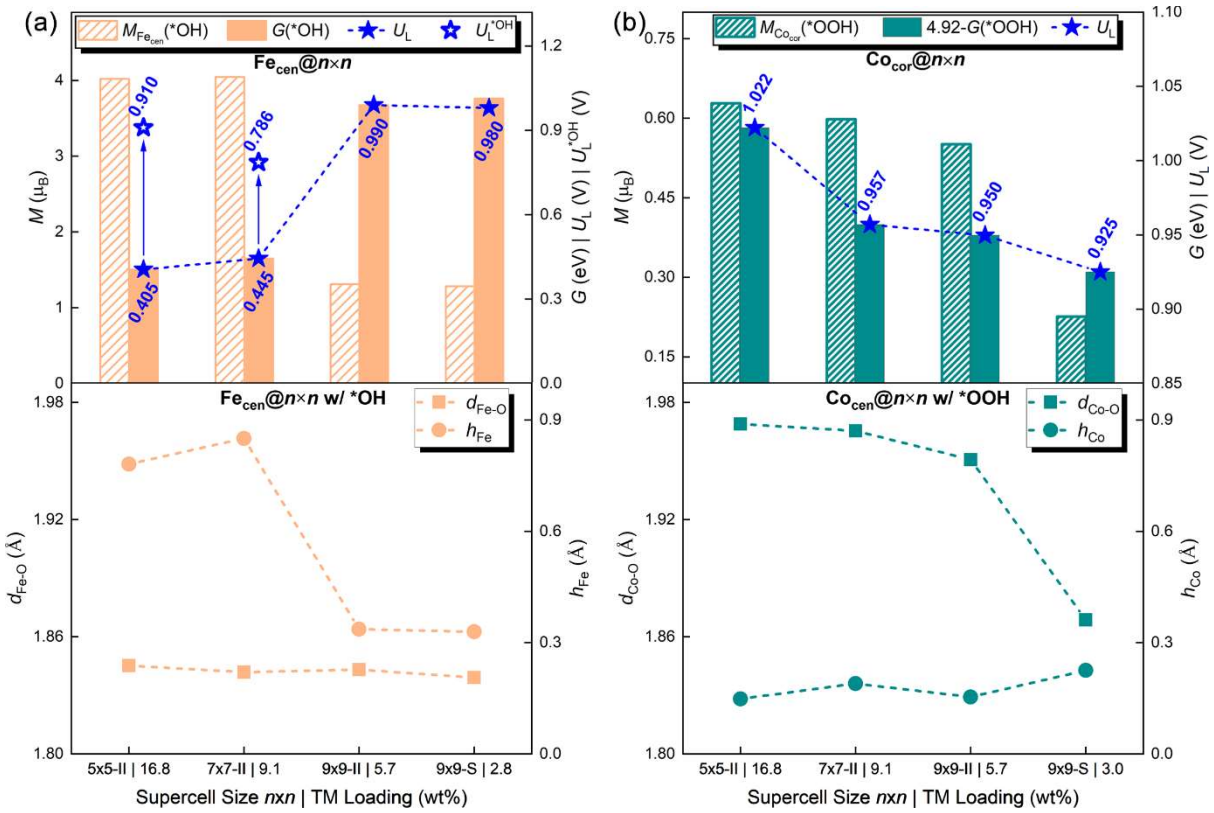


Figure 4. Top row: The Gibbs free energy of (a) *OH ($G(*\mathrm{OH})$) and (b) *OOH adsorption ($G(*\mathrm{OOH})$), the ORR limiting potential (U_L) and the projected magnetic moment (M) on (a) $\mathrm{Fe_{cen}}@n\times n$ and (b) $\mathrm{Co_{cor}}@n\times n$, respectively. The limiting potential of the hydroxyl-passivated $\mathrm{Fe_{cen}}$ ($U_\mathrm{L}^{*\mathrm{OH}}$) is marked by the empty blue star. Bottom row: The TM-O bond length ($d_{\mathrm{TM-O}}$) and the protrusion height of TM (h_TM) in the presence of (a) the *OH adsorbate on $\mathrm{Fe_{cen}}@n\times n$ (TM=Fe) and (b) the *OOH adsorbate on $\mathrm{Co_{cor}}@n\times n$ (TM=Co), respectively.

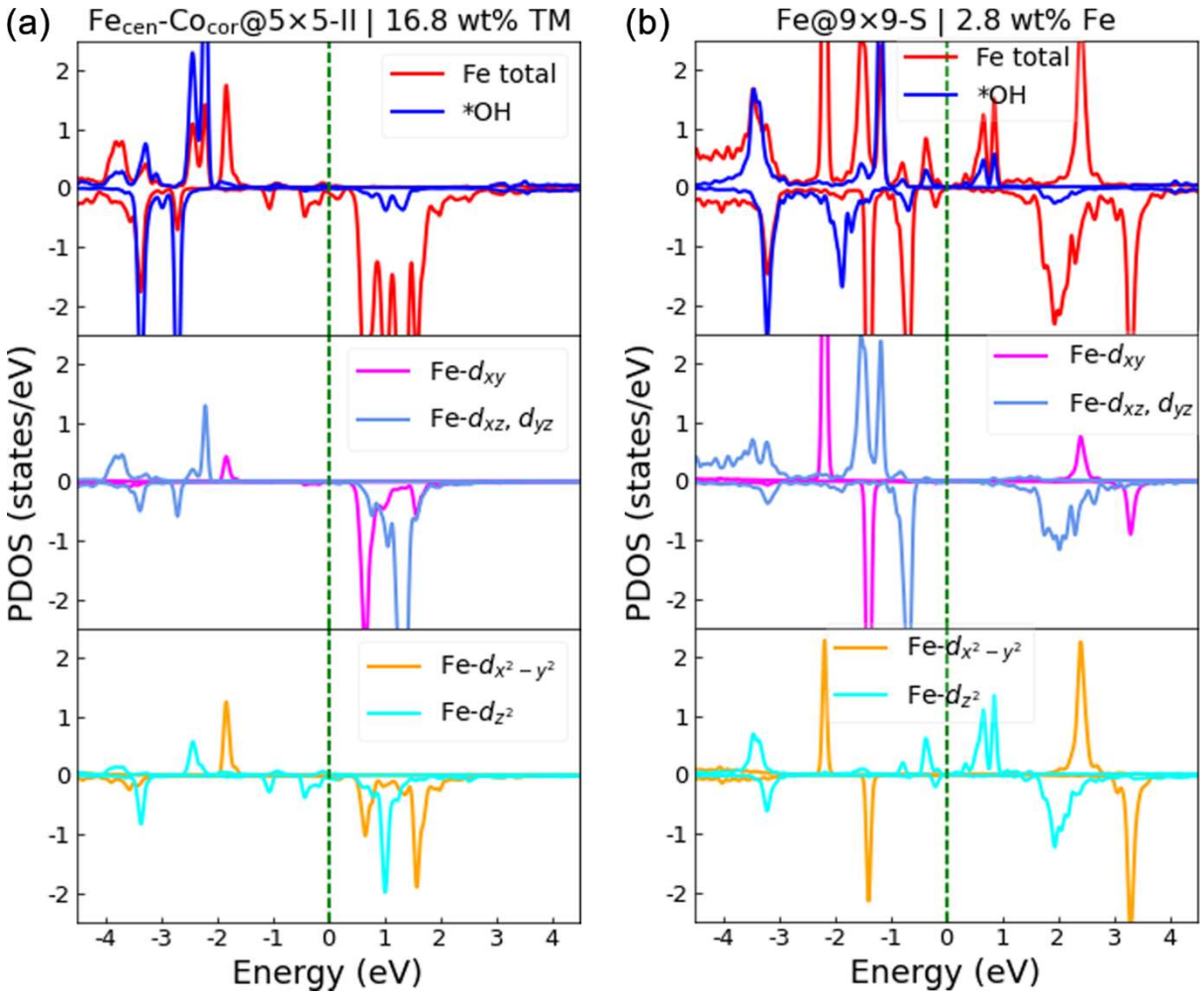


Figure 5. The projected density of states (PDOS) onto the Fe site and the *OH adsorbate of (a) Fe_{cen}-Co_{cor}@5×5-II at 16.8 wt% TM and (b) Fe@9×9-S at 2.8 wt% TM upon *OH adsorption on the Fe site. The Fermi level has been set to zero.

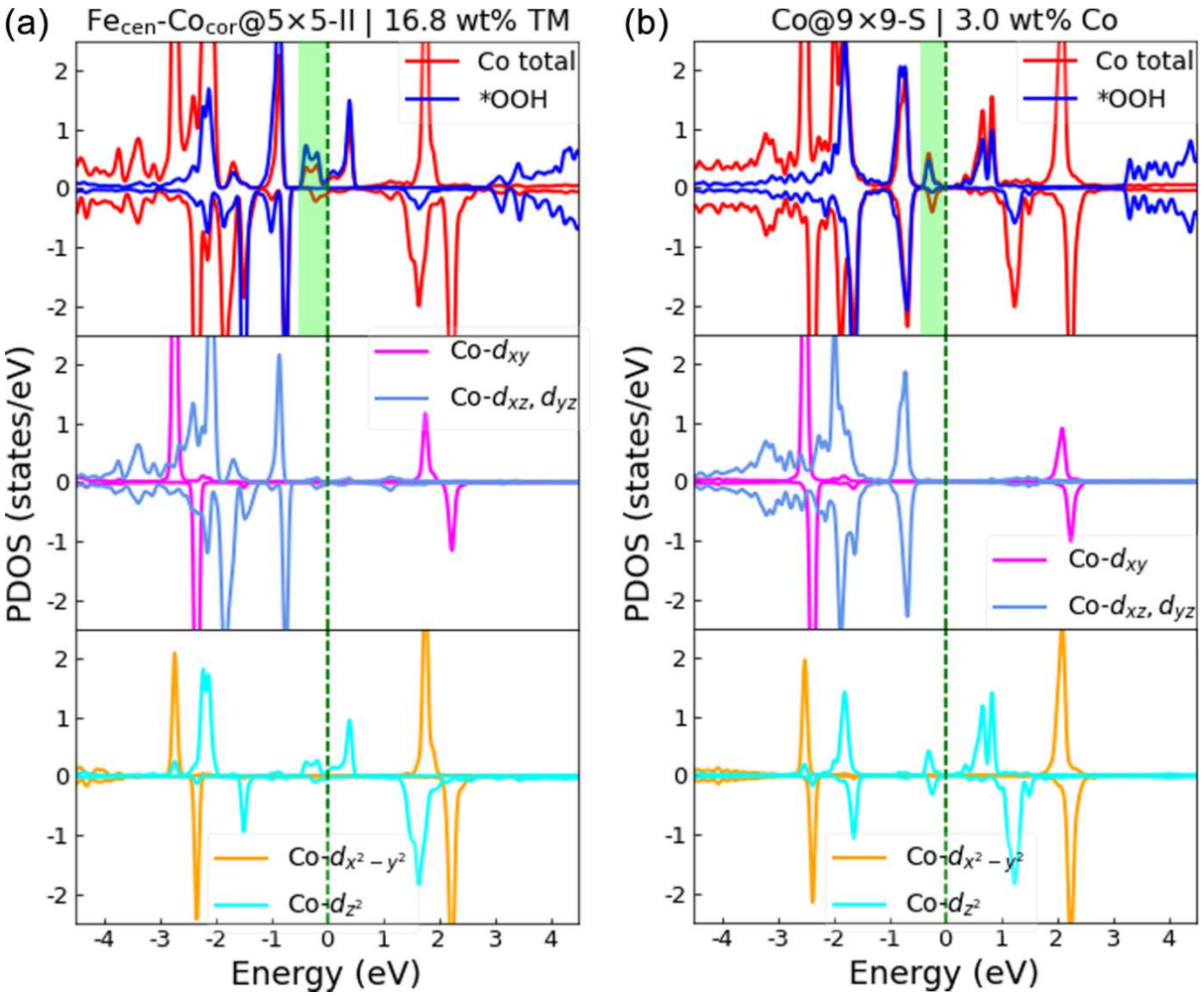


Figure 6. The projected density of states (PDOS) onto the Co site and the *OOH adsorbate of (a) Fe_{cen}-Co_{cor}@5×5-II at 16.8 wt% TM and (b) Co@9×9-S at 3.0 wt% TM upon *OOH adsorption on the Co site. The partial charge of the states in the green-shaded area is visualized in **Figure S5** in Supporting Information. The Fermi level has been set to zero.

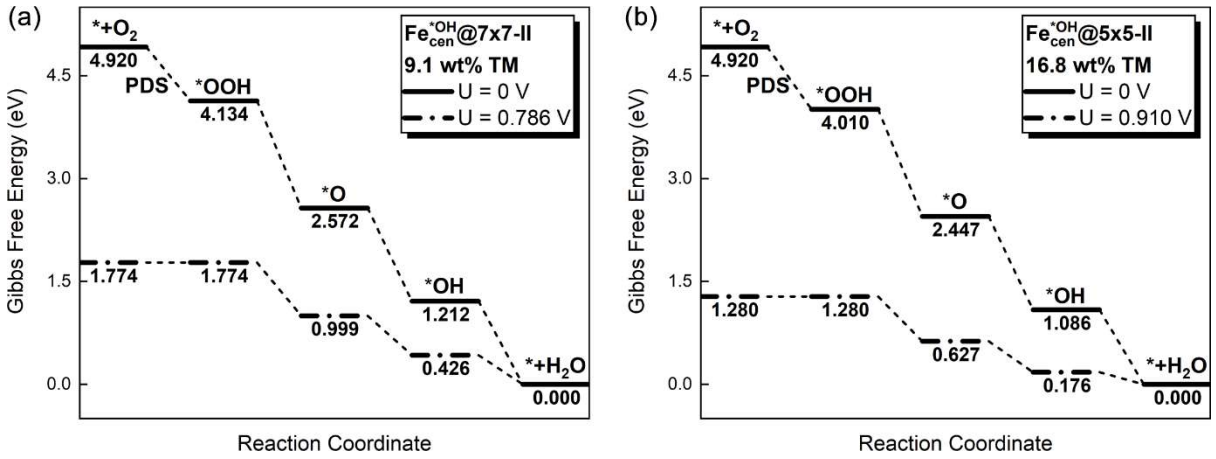


Figure 7. The oxygen reduction reaction on the hydroxyl-passivated Fe site of (a) Fe_{cen}-Co_{cor}@7×7-II and (b) Fe_{cen}-Co_{cor}@5×5-II. The corresponding TM loadings are marked.

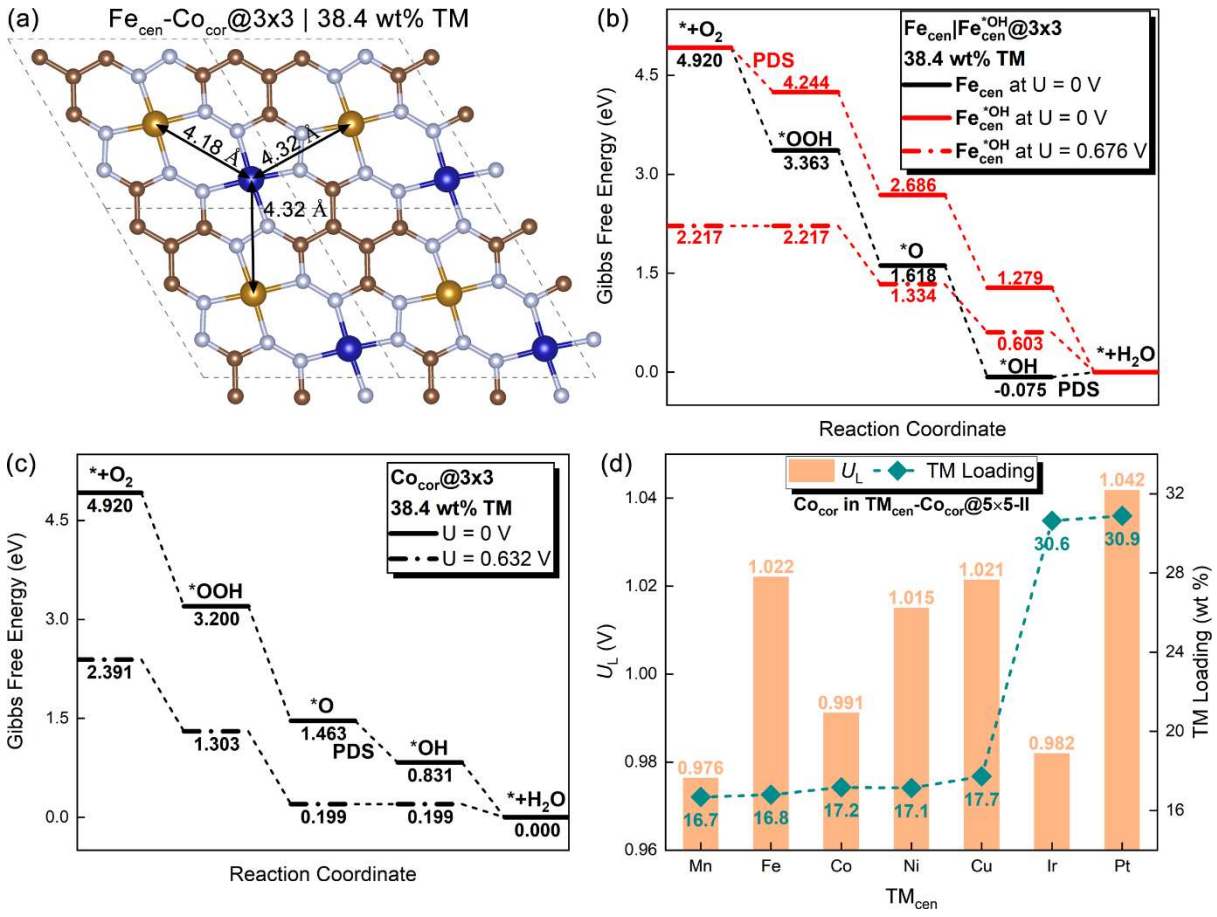


Figure 8. (a) The top view of Fe_{cen}-Co_{cor}@3×3 with the TM loading of 38.4 wt%. The distances between Fe_{cen} and Co_{cor} are marked. (b-c) The Gibbs free energy diagram for oxygen reduction reaction on (b) the Fe site (black) and the hydroxyl-passivated Fe site (red), and (c) the Co site of in-plane doubled Fe_{cen}-Co_{cor}@3×3. (d) The estimated ORR limiting potential of the Co site and the TM loading of TM_{cen}-Co_{cor}@5×5-II (TM_{cen} = Mn, Fe, Co, Ni, Cu, Ir and Pt).

References

1. R. Qin, K. Liu, Q. Wu and N. Zheng, *Chem Rev*, 2020, **120**, 11810-11899.
2. Y. Wang, H. Su, Y. He, L. Li, S. Zhu, H. Shen, P. Xie, X. Fu, G. Zhou, C. Feng, D. Zhao, F. Xiao, X. Zhu, Y. Zeng, M. Shao, S. Chen, G. Wu, J. Zeng and C. Wang, *Chem. Rev.*, 2020, DOI: 10.1021/acs.chemrev.0c00594.
3. Y. Wang, D. Wang and Y. Li, *Adv. Mater.*, 2021, **33**, 2008151.
4. W. Zang, T. Sun, T. Yang, S. Xi, M. Waqar, Z. Kou, Z. Lyu, Y. P. Feng, J. Wang and S. J. Pennycook, *Adv Mater*, 2021, **33**, e2003846.
5. Y. Xue, B. Huang, Y. Yi, Y. Guo, Z. Zuo, Y. Li, Z. Jia, H. Liu and Y. Li, *Nat. Commun.*, 2018, **9**, 1460.
6. L. Cao, Q. Luo, W. Liu, Y. Lin, X. Liu, Y. Cao, W. Zhang, Y. Wu, J. Yang, T. Yao and S. Wei, *Nat. Catal.*, 2019, **2**, 134-141.
7. S. Fang, X. Zhu, X. Liu, J. Gu, W. Liu, D. Wang, W. Zhang, Y. Lin, J. Lu, S. Wei, Y. Li and T. Yao, *Nat. Commun.*, 2020, **11**, 1029.
8. Z. Zhang, C. Feng, C. Liu, M. Zuo, L. Qin, X. Yan, Y. Xing, H. Li, R. Si, S. Zhou and J. Zeng, *Nat Commun*, 2020, **11**, 1215.
9. Y. Shi, W.-M. Huang, J. Li, Y. Zhou, Z.-Q. Li, Y.-C. Yin and X.-H. Xia, *Nat. Commun.*, 2020, **11**, 4558.
10. H. T. Chung, D. A. Cullen, D. Higgins, B. T. Sneed, E. F. Holby, K. L. More and P. Zelenay, *Science*, 2017, **357**, 479-484.
11. X. X. Wang, D. A. Cullen, Y.-T. Pan, S. Hwang, M. Wang, Z. Feng, J. Wang, M. H. Engelhard, H. Zhang, Y. He, Y. Shao, D. Su, K. L. More, J. S. Spendelow and G. Wu, *Adv. Mater.*, 2018, **30**, 1706758.
12. H. Zhang, Y. Liu, T. Chen, J. Zhang, J. Zhang and X. W. D. Lou, *Adv Mater*, 2019, **31**, e1904548.
13. J. Liu, M. Jiao, L. Lu, H. M. Barkholtz, Y. Li, Y. Wang, L. Jiang, Z. Wu, D.-j. Liu, L. Zhuang, C. Ma, J. Zeng, B. Zhang, D. Su, P. Song, W. Xing, W. Xu, Y. Wang, Z. Jiang and G. Sun, *Nat. Commun.*, 2017, **8**, 15938.
14. H. Zhou, T. Yang, Z. Kou, L. Shen, Y. Zhao, Z. Wang, X. Wang, Z. Yang, J. Du, J. Xu, M. Chen, L. Tian, W. Guo, Q. Wang, H. Lv, W. Chen, X. Hong, J. Luo, D. He and Y. Wu, *Angew. Chem. Int. Ed.* , 2020, **59**, 20465-20469.
15. W. Zang, T. Yang, H. Zou, S. Xi, H. Zhang, X. Liu, Z. Kou, Y. Du, Y. P. Feng, L. Shen, L. Duan, J. Wang and S. J. Pennycook, *ACS Catal.*, 2019, **9**, 10166-10173.
16. T. Yang, T. T. Song, J. Zhou, S. Wang, D. Chi, L. Shen, M. Yang and Y. P. Feng, *Nano Energy*, 2020, **68**, 104304.
17. C. Ling, Y. Ouyang, Q. Li, X. Bai, X. Mao, A. Du and J. Wang, *Small Methods*, 2019, **3**, 1800376.
18. Z. Geng, Y. Liu, X. Kong, P. Li, K. Li, Z. Liu, J. Du, M. Shu, R. Si and J. Zeng, *Adv. Mater.*, 2018, **30**, 1803498.
19. W. Ju, A. Bagger, G.-P. Hao, A. S. Varela, I. Sinev, V. Bon, B. Roldan Cuenya, S. Kaskel, J. Rossmeisl and P. Strasser, *Nat. Commun.*, 2017, **8**, 944.
20. D. Xi, J. Li, J. Low, K. Mao, R. Long, J. Li, Z. Dai, T. Shao, Y. Zhong, Y. Li, Z. Li, X. J. Loh, L. Song, E. Ye and Y. Xiong, *Adv Mater*, 2021, **n/a**, e2104090.
21. H. Yin, P. Yuan, B.-A. Lu, H. Xia, K. Guo, G. Yang, G. Qu, D. Xue, Y. Hu, J. Cheng, S. Mu and J.-N. Zhang, *ACS Catal.*, 2021, **11**, 12754-12762.
22. R. Jiang, L. Li, T. Sheng, G. Hu, Y. Chen and L. Wang, *J. Am. Chem. Soc.*, 2018, **140**, 11594-11598.
23. A. Han, X. Wang, K. Tang, Z. Zhang, C. Ye, K. Kong, H. Hu, L. Zheng, P. Jiang, C. Zhao, Q. Zhang, D. Wang and Y. Li, *Angew. Chem. Int. Ed.*, 2021, **60**, 19262-19271.
24. C. Tang, L. Chen, H. Li, L. Li, Y. Jiao, Y. Zheng, H. Xu, K. Davey and S.-Z. Qiao, *J. Am. Chem. Soc.*, 2021, **143**, 7819-7827.
25. E. Jung, H. Shin, B.-H. Lee, V. Efremov, S. Lee, H. S. Lee, J. Kim, W. Hooch Antink, S. Park, K.-S. Lee, S.-P. Cho, J. S. Yoo, Y.-E. Sung and T. Hyeon, *Nat. Mater.*, 2020, **19**, 436-442.
26. J. Zhang, Y. Zhao, C. Chen, Y.-C. Huang, C.-L. Dong, C.-J. Chen, R.-S. Liu, C. Wang, K. Yan, Y. Li and G. Wang, *J. Am. Chem. Soc.*, 2019, **141**, 20118-20126.

27. K. Jiang, S. Back, A. J. Akey, C. Xia, Y. Hu, W. Liang, D. Schaak, E. Stavitski, J. K. Nørskov, S. Siahrostami and H. Wang, *Nat. Commun.*, 2019, **10**, 3997.
28. X. Hai, X. Zhao, N. Guo, C. Yao, C. Chen, W. Liu, Y. Du, H. Yan, J. Li, Z. Chen, X. Li, Z. Li, H. Xu, P. Lyu, J. Zhang, M. Lin, C. Su, S. J. Pennycook, C. Zhang, S. Xi and J. Lu, *ACS Catal.*, 2020, **10**, 5862-5870.
29. X. Wan, X. Liu, Y. Li, R. Yu, L. Zheng, W. Yan, H. Wang, M. Xu and J. Shui, *Nat. Catal.*, 2019, **2**, 259-268.
30. A. Mehmood, M. Gong, F. Jaouen, A. Roy, A. Zitolo, A. Khan, M.-T. Sougrati, M. Primbs, A. M. Bonastre, D. Fongalland, G. Drazic, P. Strasser and A. Kucernak, *Nat. Catal.*, 2022, **5**, 311-323.
31. J. Li, W. Xia, J. Tang, Y. Gao, C. Jiang, Y. Jia, T. Chen, Z. Hou, R. Qi, D. Jiang, T. Asahi, X. Xu, T. Wang, J. He and Y. Yamauchi, *J. Am. Chem. Soc.*, 2022, DOI: 10.1021/jacs.2c00719.
32. X. Hai, S. Xi, S. Mitchell, K. Harrath, H. Xu, D. F. Akl, D. Kong, J. Li, Z. Li, T. Sun, H. Yang, Y. Cui, C. Su, X. Zhao, J. Li, J. Pérez-Ramírez and J. Lu, *Nat. Nanotechnol.*, 2021, DOI: 10.1038/s41565-021-01022-y.
33. Z. Jin, P. Li, Y. Meng, Z. Fang, D. Xiao and G. Yu, *Nat. Catal.*, 2021, **4**, 615-622.
34. L. Han, H. Cheng, W. Liu, H. Li, P. Ou, R. Lin, H.-T. Wang, C.-W. Pao, A. R. Head, C.-H. Wang, X. Tong, C.-J. Sun, W.-F. Pong, J. Luo, J.-C. Zheng and H. L. Xin, *Nat. Mater.*, 2022, DOI: 10.1038/s41563-022-01252-y.
35. R. Hu, Y. Li, Q. Zeng and J. Shang, *Applied Surface Science*, 2020, **525**, 146588.
36. X. Guo, S. Lin, J. Gu, S. Zhang, Z. Chen and S. Huang, *ACS Catal.*, 2019, **9**, 11042-11054.
37. H. Peng, F. Liu, X. Liu, S. Liao, C. You, X. Tian, H. Nan, F. Luo, H. Song, Z. Fu and P. Huang, *ACS Catal.*, 2014, **4**, 3797-3805.
38. J. Wang, Z. Huang, W. Liu, C. Chang, H. Tang, Z. Li, W. Chen, C. Jia, T. Yao, S. Wei, Y. Wu and Y. Li, *J. Am. Chem. Soc.*, 2017, **139**, 17281-17284.
39. J. Wang, W. Liu, G. Luo, Z. Li, C. Zhao, H. Zhang, M. Zhu, Q. Xu, X. Wang, C. Zhao, Y. Qu, Z. Yang, T. Yao, Y. Li, Y. Lin, Y. Wu and Y. Li, *Energy Environ. Sci.*, 2018, **11**, 3375-3379.
40. X.-F. Li, Q.-K. Li, J. Cheng, L. Liu, Q. Yan, Y. Wu, X.-H. Zhang, Z.-Y. Wang, Q. Qiu and Y. Luo, *J. Am. Chem. Soc.*, 2016, **138**, 8706-8709.
41. J. Hwang, R. R. Rao, L. Giordano, Y. Katayama, Y. Yu and Y. Shao-Horn, *Science*, 2017, **358**, 751-756.
42. F. Li, H. Ai, D. Liu, K. H. Lo and H. Pan, *J. Mater. Chem. A*, 2021, **9**, 17749-17759.
43. U. I. Kramm, M. Lefèvre, N. Larouche, D. Schmeisser and J.-P. Dodelet, *J. Am. Chem. Soc.*, 2014, **136**, 978-985.
44. X. Li, C.-S. Cao, S.-F. Hung, Y.-R. Lu, W. Cai, A. I. Rykov, S. Miao, S. Xi, H. Yang, Z. Hu, J. Wang, J. Zhao, E. E. Alp, W. Xu, T.-S. Chan, H. Chen, Q. Xiong, H. Xiao, Y. Huang, J. Li, T. Zhang and B. Liu, *Chem*, 2020, **6**, 3440-3454.
45. W. Zhong, Y. Qiu, H. Shen, X. Wang, J. Yuan, C. Jia, S. Bi and J. Jiang, *J Am Chem Soc*, 2021, **143**, 4405-4413.
46. G. Yang, J. Zhu, P. Yuan, Y. Hu, G. Qu, B.-A. Lu, X. Xue, H. Yin, W. Cheng, J. Cheng, W. Xu, J. Li, J. Hu, S. Mu and J.-N. Zhang, *Nat. Commun.*, 2021, **12**, 1734.
47. B. Hu, A. Huang, X. Zhang, Z. Chen, R. Tu, W. Zhu, Z. Zhuang, C. Chen, Q. Peng and Y. Li, *Nano Res.*, 2021, DOI: 10.1007/s12274-021-3535-4.
48. F. Li, G.-F. Han, H.-J. Noh, S.-J. Kim, Y. Lu, H. Y. Jeong, Z. Fu and J.-B. Baek, *Energy Environ. Sci.*, 2018, **11**, 2263-2269.
49. M. Xiao, J. Zhu, G. Li, N. Li, S. Li, Z. P. Cano, L. Ma, P. Cui, P. Xu, G. Jiang, H. Jin, S. Wang, T. Wu, J. Lu, A. Yu, D. Su and Z. Chen, *Angew. Chem. Int. Ed.*, 2019, **58**, 9640-9645.